CHEMIJA. 2013. Vol. 24. No. 2. P. 128–136

Theoretical and experimental studies of layer by layer nucleation and growth of palladium on stainless steel 316L

Iman Danaee*

Abadan Faculty of Petroleum Engineering, Petroleum University of Technology, Abadan, Iran

Palladium nucleation and growth from 0.01 M $Pd(NH_3)_4Cl_2$, NH_4Cl, and NH_4OH bath (pH = 10) are studied by means of cyclic voltammetry (CV), impedance spectroscopy (EIS) and electrochemical noise (EN). Crossovers in cyclic voltammograms demonstrate that the deposition of palladium proceeds via a nucleation / growth mechanism. A model based on random birth and deterministic growth of monolayers is proposed, in which the edges are assumed to follow a propagation law. The high frequency impedance data show charge transfer reaction of Pd^{2+} reduction while the low frequency features signify the growth mode of deposits. The inductive response observed in the course of polycrystalline deposition reflects the activation of electrode area while a capacitive loop appears in regular growth. Kinetic parameters of the impedance model in this system can be calculated from the fitting of experimental data to the Faradaic impedance function derived theoretically. The physical parameters of this function are analyzed by means of the dependence of simulated EIS spectra on kinetic parameters. The electrochemical noise is shown to originate from the random birth of edges and therefore the birth rate of monolayers was lower than $4.7 \times 10^{16} s^{-1}\ cm^{-2}$.

Key words: palladium, impedance, noise, Adatom model, electrocrystallization

INTRODUCTION

Palladium has excellent physical and chemical properties such as corrosion and wear resistance, thermal stability, and high catalytic activity for various chemical reactions, so that it is mainly used for industrial applications like catalysis and electrical devices [1, 2]. Palladium thin films deposited on gold and platinum substrates demonstrate extremely high catalytic activities in the electrooxidation reaction of small organic molecules such as formaldehyde and formic acid [3–5]. The electrodeposition of palladium has been studied on various electrodes such as graphite, polymer matrix, and porous stainless steel electrode [6–9]. The electrochemical layer-by-layer growth of palladium was reported on copper and a gold single crystal electrode [10–12]. Electrodeposition of metal on steel substrate has received some attention by several authors [13, 14]. Steel modified with metal and alloy has been used for electrocatalytic reaction in fuel cell, battery and hydrogen separation [15, 16].

Electrochemical impedance spectroscopy (EIS) is an example of frequency response analysis which has proved to be useful in both applied and fundamental electrochemical studies [17–19] as well as in other disciplines [20]. The power of the technique is its ability to distinguish among the interfacial processes with different time constants [21]. EIS is a common and useful technique for studying metals electrocrystallization [22–26]. One of its advantages is the possibility of studying the relaxation of the electrode surface

* Corresponding author. E-mail: danaee@put.ac.ir

from adsorbed species and growth of layers. The impedance spectra of the deposition processes of metals usually show one or several relaxations (capacitive or inductive) [27]. The surface diffusion of Adatoms can also be a determining step in the overall mechanism of electrocrystallization (Adatoms model) [28–31]. Two dimensional nucleation and growth and the interactions between growth centers have been extensively studied [32–35]. The impedance characteristic of the response of the deposition successive layers to potential steps of a small amplitude has also been studied [36, 37]. It is known that the formation and development of growth centers during electrodeposition can give rise to a variation of the active area of the electrode and the subsequent changes of the process overpotential. It has been shown that the relaxation of the active area can generate either an inductive or a capacitive loop characterized by distributed time constants [38]. From a different approach based on the assumption of successive monolayers randomly generated and obeying a given ageing law, an analytical expression for the electrode impedance has been derived [38].

The impedance model construction is frequently the final aim of an experimental impedance study [39]. As the aim of impedance modeling is knowledge enhancement, the applied models should possess physical significance, i. e. they should correspond to the structure and the properties of processes taking place in the system under study [40, 41]. The parameters identification can be made by using these impedance models that give important information about the influence of the physical parameters [42–45].

Electrochemical noise measurements have traditionally been analyzed in the frequency domain using power spectral density plots by means of fast Fourier transform (FFT). Xiao and Mansfeld [46, 47] have extended the analysis in the frequency domain by introducing spectral noise plots in which the ratio of the FFT of potential and current noise is plotted as a function of frequency in the Bode plot format. Therefore, it has some analogy with the modulus of the electrode impedance. During metal electrodeposition, the electrochemical dynamical parameters, such as current and potential, will fluctuate spontaneously, which has been designated as electrocrystallization noise [48–50]. It was shown by Budevski et al. [51, 52] that a well-defined electrocrystallization system under constant cathodic overpotential or current exhibit fluctuations which should contain more information on the 2D nucleation and crystal growth process than commonly expected.

The aim of this work is the analysis of impedance and noise characteristics of the palladium electrocrystallization process from 0.01 M $Pd(NH_3)_4Cl_2$, NH_4Cl, and NH_4OH on a stainless steel 316L substrate. The analysis of the theoretical impedance function provides important information on the process parameters. This information allows the EIS spectrum simulation and, therefore, predicts the system behavior with regard to the variation of the experimental conditions.

EXPERIMENTAL

Materials used in this work were analytical grade of Merck origin. The experiments were carried out in a conventional three-electrode cell containing 0.01 M $Pd(NH_3)_4Cl_2$, 0.04 M NH_4Cl and 0.3 M NH_3 at 25 °C. The working electrode was a stainless steel 316L rod mounted in Teflon with an apparent exposed area of 0.25 cm^2. Its potential was monitored against an Ag/AgCl reference electrode. A large graphite rod was used as the counter electrode.

Prior to each experiment, the surface pretreatment of the working electrode was performed by hand polishing of the electrode surface with successive grades of emery papers down to 3 000 grit up to a mirror finish. The polished electrode was then degreased with acetone and washed with running, doubly distilled water.

The methods of cyclic voltammetry, impedance spectroscopy were powered by a EG & G model 273A potentiostat / galvanostat and Solartron model 1255 frequency response analyzer runs by a PC through M270 and M398 software. Electrochemical noise measurements were performed by a potentiostat / galvanostat Solarton model 1266. The system is run through CorrWare, commercial software. The frequency range of 100 kHz to 15 mHz and the modulation amplitude of 5 mV were employed for impedance measurements. Fitting of experimental impedance spectroscopy data to the proposed equivalent circuit was done by means of home written least square software based on the Marquardt method for the optimization of functions and Macdonald weighting for the real and imaginary parts of the impedance [53, 54].

RESULTS AND DISCUSSION

Cyclic voltammogram obtained in the potential range of 0 to –1.3 V vs. Ag/AgCl with a scan rate of 100 mV s^{-1} is presented in Fig. 1. During the scan in the cathodic direction, significant crystallization overpotential can be noticed before palladium electrodeposition occurs; the cathodic current density increases at potential more negative than –0.74 V. The reduction peak is observed at –1.17 V and, at more negative potential, current density increases again due to the hydrogen evolution. The reverse scan shows initially a decrease in current density, and two crossovers are observed, one at more negative than crystallization potential and the other at zero current, characteristic of metal deposition onto substrates of different nature. From Fig. 1, equilibrium potential of the system can be obtained as –0.53 V vs. Ag/AgCl. On reversing the scan direction, metal already deposited on the electrode surface continues to grow as a result of the deposition reaction remaining thermodynamically and kinetically favorable. In the following reverse scan, at more positive potential, an anodic peak appears which is associated with the stripping of Pd formed during the scan in negative direction. The relative location of the deposition and stripping signals suggest a complex irreversible type identified by Fletcher [55, 56].

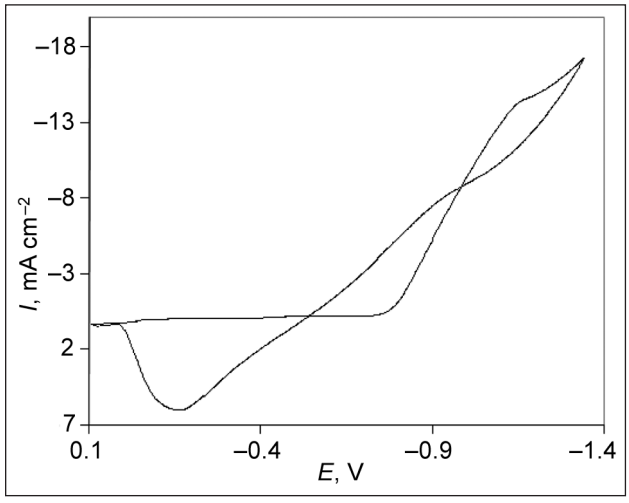

Fig. 1. The first cycle of voltammogram of the palladium electrodeposition from 0.01 M $Pd(NH_3)_4Cl_2$, NH_4Cl, and NH_4OH bath. The scan begins at 0.2 V vs. Ag/AgCl with a scan rate of 100 mV s^{-1}

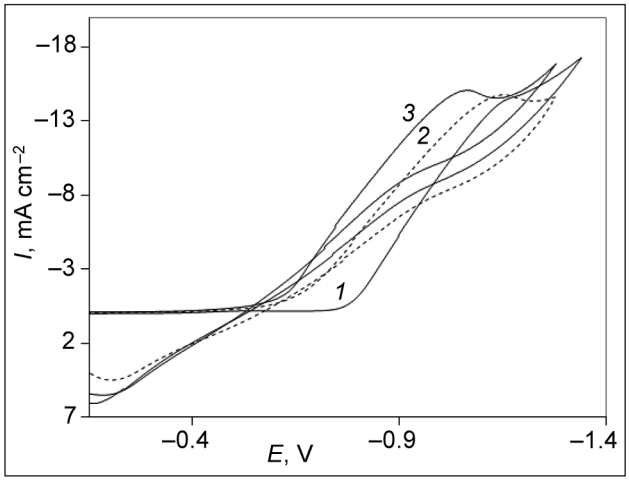

Fig. 2. Consecutive cyclic voltammograms of the palladium electrodeposition with a scan rate of 100 mV s^{-1}: *1* – the first cycle, *2* – the third one and *3* – the fifth cycle

Integration of both cathodic and anodic peaks gave a charge ratio $Q_c/Q_a > 1$. This behavior was already observed in other systems [57] and explained in terms of a residual metal deposit on the electrode surface. After further cycling, lower crystallization overpotential is needed before palladium electrodeposition occurs (Fig. 2). This indicates that residual palladium deposit after each scan promotes the nucleation and deposition of palladium in the following cathodic cycle.

Fig. 3a presents Nyquist plots of steel electrode for palladium deposition recorded at various applied cathodic potential steps in the range of –0.81 to –0.93 V vs. Ag/AgCl. The Nyquist diagrams consist of two slightly depressed capacitive semicircles in high and medium frequencies and one inductive loop in low frequencies. As can be seen, increasing applied cathodic overpotential decreases the diameters of capacitive semicircles. Bode phase plots for the same sample are shown in Fig. 3b. Three distinguishable peaks with positive

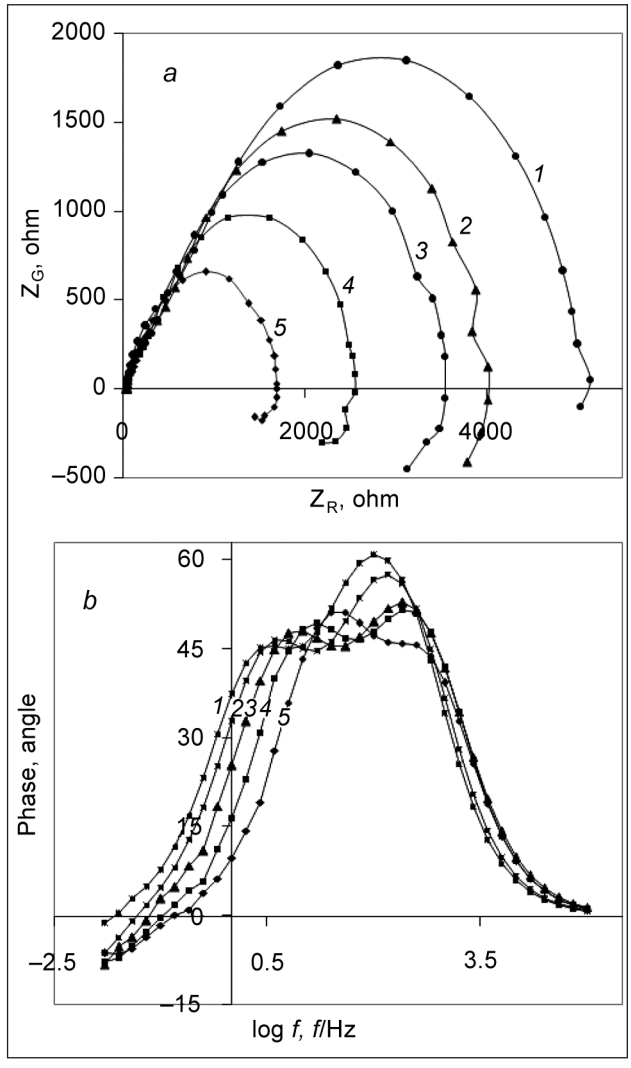

Fig. 3. Experimental (*a*) Nyquist diagrams (*b*) phase shift plots measured for deposition of palladium on steel at different cathodic potential: *1* – –0.81, *2* – –0.84, *3* – –0.87, *4* – –0.9 and *5* – –0.93 V vs. Ag/AgCl

and negative phase angles are observed in the Bode plots corresponding capacitive and inductive loops in Nyquist plots. The complex plane plots exhibit fast electron-transfer and two relaxation processes characterized by distributed time constant. At high frequency, the distorted capacitive loop is related to the charge transfer resistance in parallel with double-layer capacitance. At low frequency, distorted capacitive and inductive loops are observed which are characteristics of nucleation and growth of metal [38, 58]. The processes give rise to change in the active area of the substrate surface. Nucleation of palladium leads to generation and propagation of growth edges on the surface and further growth of nuclei will take place through edges advancement.

Faradaic impedance function

On the growth sites Me* provided by nucleation, metal deposition occurs through electron transfer

$$Me^* + Me^{n+} + ne \rightleftharpoons Me + Me^*, \quad (1)$$

The growth of two-dimensional nuclei will take place through edges advancement with the rate ν [23]:

$$\nu = \frac{MJ}{\rho F}, \tag{2}$$

where M is the atomic weight and ρ is the density of the deposit.

In this model, an active edge of the height h is considered to propagate at the rate of $\nu = dr/dt$ which is proportional to the growth current density J when the discharge and incorporation of ions are assumed to take place simultaneously on the growth sites [59]. r is the distance of propagation and the edge length $l = l_0 f(u,\tau)$ is defined from the ageing law $f(u, \tau)$, where $u = r/\nu$ is the monolayer age and τ denotes the life-time elapsed when the monolayer attains its maximal size $l_m = l_0 max[f(u, \tau)]$ for a propagation distance r_0 such that [59]

$$\tau = \frac{r_0}{\nu} = \int_0^\infty f\,(u,\tau)\,\mathrm{d}u. \tag{3}$$

The successive monolayers have been assumed to be generated at a mean nucleation rate and to follow the same ageing law as nuclei formed at random in time and space [38].

If h is the height of edges, the elementary current-time transient due to the development of one edge is [38]

$$i(u) = Jhl_0 f(u,\tau). \tag{4}$$

At time t the total current $I(t)$ is

$$I(t) = \sum_n i(t - t_n), \tag{5}$$

where t-t_n is the age of monolayer.

The current for metal deposition is thus given by the following equation[59]:

$$I(t) = JhL = Jhl_0 \int_0^\infty f(r, r_0)\frac{m}{\nu}\left(t - \frac{r}{\nu}\right)\mathrm{d}r, \tag{6}$$

where m is the nucleation rate, m/ν is the size distribution function of edges and L denotes the total length of edges.

For a small perturbation of overpotential from steady state conditions, the current variation is [24]

$$\begin{aligned}\Delta I(t) = {} & \Delta J(t) hl_0 \frac{mr_0}{\nu} + Jhl_0 \int_0^\infty g(r, r_0)\,\Delta\frac{m}{\nu} \\ & \left(t - \frac{r}{\nu}\right)\mathrm{d}r + Jhl_0 \int_0^\infty \Delta g(r, r_0)\frac{m}{\nu}\left(t - \frac{r}{\nu}\right)dr.\end{aligned} \tag{7}$$

Then the steady-state current and the Faradaic impedance Z_F were obtained as follows [59]:

$$I = Jhl_0 m\tau; \tag{8}$$

$$Z_F^{-1} = R_t^{-1} + ihl_0 m\left(\frac{\Delta m}{m\Delta E} - \frac{\Delta\nu}{\nu\Delta E}\right)F(w), \tag{9}$$

where E is the electrode potential and the charge transfer resistance, R_t, and the Fourier transform of the aging function, $F(w)$, are given by the following equations, respectively:

$$R_t^{-1} = \left(\frac{\partial I}{\partial E}\right)_L \tag{10}$$

$$\text{and [59]}\ F(w) = \int_0^\infty f(u,\tau)\exp(-jwu)\,\mathrm{d}u. \tag{11}$$

Whereas J and E are considered to vary in phase, Δm can be reasonably assumed to be retarded. The establishment of the steady state nucleation rate occurs partially with retardation and therefore [38]

$$\frac{\Delta m}{\Delta\eta} = \frac{dm}{d\eta}\left(\frac{\lambda}{1 + jw\tau_n} + 1 - \lambda\right), \tag{12}$$

where $dm/d\eta$ is the steady state variation and λ denotes the fraction of nuclei that needs the delay time τ_n before entering into the ageing process. This induction time includes the relaxation time of nucleation and every possible retarding event such as the relaxation of intermediates or desorption of inhibiting adsorbates. For a simple ageing function [59]

$$f(u,\tau) = \frac{u}{\tau}\exp\left(-\frac{u}{\tau}\right) \tag{13}$$

the Fourier transform is [38]

$$F(w) = \frac{\tau}{(1 + jw\tau)^2}. \tag{14}$$

This function is similar to the potentiostatic transients corresponding to the instantaneous nucleation and growth of a 2-D layer [33].

Finally Z_F becomes the following function of the two time-constant τ and τ_n:

$$\begin{aligned}Y_F = {} & \frac{1}{Z_F} = \frac{1}{R_t} + \frac{a_2\lambda}{a_1 R_P a_4} + \frac{a_2 a_3}{a_1} - \\ & - \frac{\omega^2\tau\tau_n\lambda}{a_1 R_P a_4} - \frac{\omega a_2\tau_n\lambda j}{a_1 R_P a_4} - \frac{\omega\tau\lambda j}{a_1 R_P a_4} - \frac{\omega a_3\tau j}{a_1},\end{aligned} \tag{15}$$

$$a_1 = 2\omega^2\tau^2 = \omega^4\tau^4 + 1,$$

$$a_2 = (1 - \omega^2\tau^2),$$

$$a_3 = \left(\frac{1}{R_P} - \frac{\lambda}{R_P} - \frac{1}{R_t}\right),$$

$$a_1 = (1 - \omega^2\tau_n{}^2).$$

The delay τ_n including both the induction time for nucleation [59] and any retarding event such as the slow desorption of inhibiting species and λ denotes the fraction of nuclei that needs the delay time τ_n before entering into the ageing process. In Equation (15), the charge transfer resistance is R_t and the polarization resistance is designated as R_P.

In this case, the multilayer formation has been treated as a cascade process, in which the (n + 1)-th layer is borne out of the n-th layer so that the current can be evaluated by

Table 1. **Equivalent circuit parameters of palladium electrocrystallization on stainless steel 316L electrode obtained from Fig. 2**

E, V	R_s, Ω	$R_t \times 10^{-2}$, Ω	$R_p \times 10^{-3}$, Ω	$Q_{dl} \times 10^5$, F	τ, s	$\tau_n \times 10^{-2}$, s	λ	n_{dl}
–0.81	35	11.38	2.55	8.05	0.05	5.8	0.51	0.88
–0.84	35	8.05	2.81	7	0.03	3.5	0.43	0.88
–0.87	34	6.15	2.1	5.95	0.03	1.9	0.4	0.87
–0.9	34	4.43	1.55	5.02	0.018	0.9	0.38	0.87
–0.93	35	2.63	1.1	8	0.01	0.67	0.35	0.87

a recurrence relationship. Such an approach to multilayer formation implies both the birth (by nucleation) and the death (as a consequence of overlap) of each monolayer. In Fig. 3, two relaxation processes show up, one (with time constant τ_n) due to the retardation of nucleation, the other (roughly speaking with time constant τ) is a result of the propagation of edges. In this analysis of the birth and growth of monolayers, it seems that at intermediate frequencies the capacitive feature originates from the propagation of edges over a finite distance, whereas at low frequencies the inductive response essentially reflects the relaxation of intermediates or slow desorption of inhibiting adsorbates which allows the edges to propagate over a longer distance.

To corroborate this equation, Eq. (15) is fitted to the experimental data in the applied potential interval of –0.81 to –0.93 V vs. Ag/AgCl, and taking into account the double layer capacitance. These fittings agree with the experimental data. The evolution of the impedance parameters with respect to the applied potential is consistent with the model, Table 1. It is observed that all impedance parameters decrease with increasing cathodic potential. The retardation time τ_n necessary for the propagation distance to be lengthened decreases with increasing overpotential showing that in higher potential induction time for nucleation is lower and desorption of inhibiting species is faster and also that the fraction of nuclei that need τ_n is diminished. The time constant τ that decreases with overpotential indicates that the mean life-time of edges is lower in higher overpotential and a monolayer promptly attains its maximal size and that a complete monolayer forms at a faster rate at higher overpotentials [60]. The $\ln R_{ct}$ is linear versus different cathodic potential which is an indication of the prevalence of charge transfer process at the high frequency side of the impedance spectrum. The values of obtained charge transfer resistance for palladium electrodeposition were high due to low applied cathodic overpotential in the nucleation and growth region.

The characteristic points are the singular points of the Faradaic impedance function and their calculation can provide interesting information on the impedance parameters of the system. When the frequency tends to infinity (initial point of the first loop), the Faradaic impedance as given by Equation (15) shows the following value for the characteristic point:

$$Z_{\text{imag}}^{w\to\infty} = 0, \tag{16}$$

$$Z_{\text{real}}^{w\to\infty} = R_s, \tag{17}$$

where R_s is solution resistance. On the other hand, when the frequency tends to zero, the Faradaic impedance Z_F coincides with the polarization resistance R_p and is also obtained from the theoretical Faradaic impedance function:

$$Z_{\text{imag}}^{w\to 0} = 0, \tag{18}$$

$$Z_{\text{real}}^{w\to 0} = R_P. \tag{19}$$

The third case is characterized by the fact that the imaginary part of the Faradaic impedance is zero. Thus, in this situation, the frequency value in the low frequency end of the spectrum depends on all impedance parameters:

$$\omega^{Z_{\text{imag}}=0} = \frac{\sqrt{-\tau\tau_n(\lambda\tau R_t - \tau_n R_t + \lambda\tau_n R_t + R_P\tau_n)(-\lambda\tau_n R_t + \tau R_P - \tau R_t)}}{\lambda\tau_n R_t\tau^2 - \tau R_t\tau_n^2 + \tau\lambda R_t\tau_n^2 + \tau R_P\tau_n^2}. \tag{20}$$

A hierarchically distributed equivalent circuit for simulating Pd^{2+} reduction and Pd crystallization is reproduced in Fig. 4 on the basis of the adatom model [28–31]. The adatom model assumes that the metal ions are discharged onto the electrode surface and then, after diffusion along the electrode surface, the adatoms are incorporated into the metal at growth sites located at the edges of nucleus. To obtain a satisfactory impedance simulation of Pd^{2+} reduction, it is necessary to replace the capacitor, *C*, with a constant phase element (*CPE*) *Q* in the equivalent circuit. The impedance of the *CPE* element is defined as $Z_{CPE} = 1/C(j\omega)^n$ and the interpretation of this element depends on the *n* values [61]. The most widely ac-

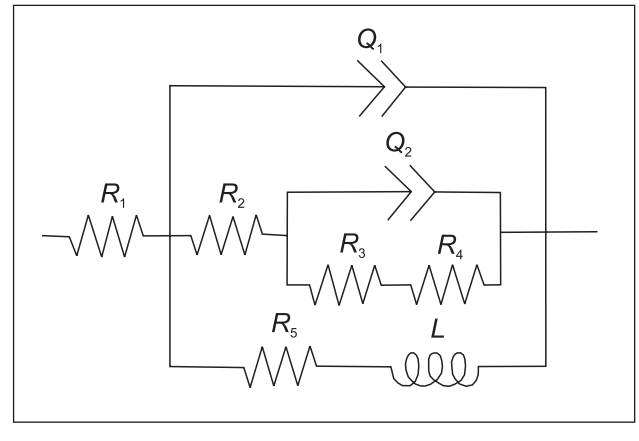

Fig. 4. Equivalent circuits compatible with the experimental impedance data in Fig. 2 for palladium electrocrystallization on stainless steel 316L electrode

cepted explanation for the presence of *CPE* behavior and depressed semicircles on solid electrodes is microscopic roughness, causing an inhomogeneous distribution in the solution resistance as well as in the double-layer capacitance [62]. In this electrical equivalent circuit, R_1, CPE_1 and R_2 represent solution resistance, a constant phase element corresponding to the double layer capacitance and the charge transfer resistance. R_3, R_4 and R_5 are the electrical elements related to the surface diffusion resistance, lattice formation resistance and inductor's resistance, respectively. Also, CPE_2 and L are due to surface diffusion capacitance and inductance. In this circuit, the charge transfer resistance of the electrode reaction is the circuit element that has a simple physical meaning describing how fast the rate of charge transfer during palladium electrodeposition changes with changing electrode potential when the surface coverage is held constant.

The values of the circuit elements of the considered equivalent circuit (Fig. 4) derived by fitting experimental data to the equivalent circuit at various dc-offset potentials are presented in Table 2. As can be seen, increasing applied cathodic overpotential decreases the diameters of two capacitive semicircles.

Comparing the theoretical faradaic crystallization impedance, Eq. (15), and the equivalent circuit, the relations between the resistances R_t, R_p and the equivalent circuit elements are established. These relations are shown in the following system of equations:

$$R_t = R_2, \tag{21}$$

$$PSD_{I,e} = \frac{PSD_{V,e}}{|Z|^2}, \tag{22}$$

which are in agreement with the data presented in Tables 1 and 2.

EIS dependence on parameter λ and τ

The fraction of nuclei which need the induction time τ_n has influences on both the capacitive and the inductive loops appearing in the intermediate and high frequency domains, Fig. 5. So, as this parameter decreases, the size of both loops decreases. As can be seen, with decreasing λ, the value of resistances R_3 and R_4 also decreases indicating lower surface diffusion and lattice formation resistance. For low value of λ the propagation of edges and monolayer formation are fast and in agreement with the low resistance R_3 and R_4.

Fig. 6 presents complex plane plots derived at different value of τ. It can be seen that the main effect of τ variation is on CPE_2 and as this parameter decreases, the value of capacitance decreases in agreement with Table 1.

Electrochemical noise measurements

The electrochemical noise analysis provides additional information. Fig. 7 show the power spectral density, PSD, plot of potential noise for Pd electrocrystallization on the steel electrode in different applied cathodic currents. Very high

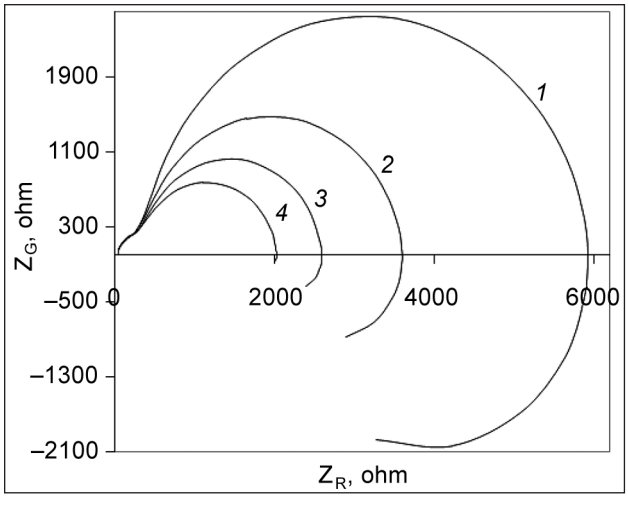

Fig. 5. Simulated diagrams for the evolution of the EIS spectrum with regard to the λ variation. The impedance parameters: $R_{ct} = 600\ \Omega$, $R_p = 1\,800\ \Omega$, $\tau = 0.1$ s, $\tau_n = 150$ s, $Q_{dl} = 0.00006$ F, $n_{dl} = 0.88$, $R_s = 30\ \Omega$, $\lambda_1 = 0.7$, $\lambda_2 = 0.5$, $\lambda_3 = 0.3$, $\lambda_4 = 0.1$

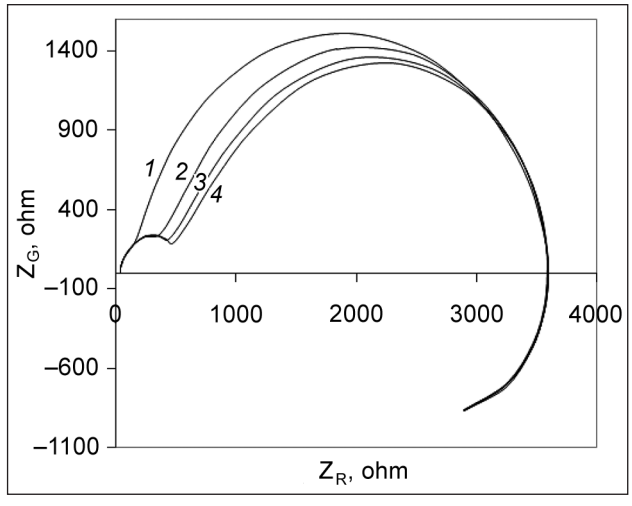

Fig. 6. Simulated diagrams for the evolution of the EIS spectrum with regard to the τ variation. The impedance parameters: $R_{ct} = 600\ \Omega$, $R_p = 1\,800\ \Omega$, $\lambda = 0.02$, $\tau_n = 150$ s, $Q_{dl} = 0.00006$ F, $n_{dl} = 0.88$, $R_s = 30\ \Omega$, $\tau_1 = 0.01$ s, $\tau_2 = 0.04$ s, $\tau_3 = 0.07$ s, $\tau_4 = 0.1$ s

Table 2. **Impedance parameters calculated from the fitting of Eq. (15) to the experimental data of Fig. 2**

E, V	R_1, Ω	$R_2 \times 10^{-2}$, Ω	$Q_1 \times 10^5$, F	$(R_3 + R_4) \times 10^{-3}$, Ω	$Q_2 \times 10^4$, F	$R_5 \times 10^{-3}$, Ω	$L \times 10^{-5}$, H	n_1	n_2
–0.81	34	11.54	8	3.9	2.51	13.5	85.4	0.88	0.86
–0.84	35	8.02	7.1	3.27	2.22	11.51	15.1	0.88	0.88
–0.87	35	6.12	6.1	2.99	1.5	9.3	8.1	0.85	0.88
–0.9	34	4.48	5	2.11	1.2	7.52	4.9	0.87	0.87
–0.93	35	2.61	5	1.42	0.9	6.05	3.1	0.88	0.87

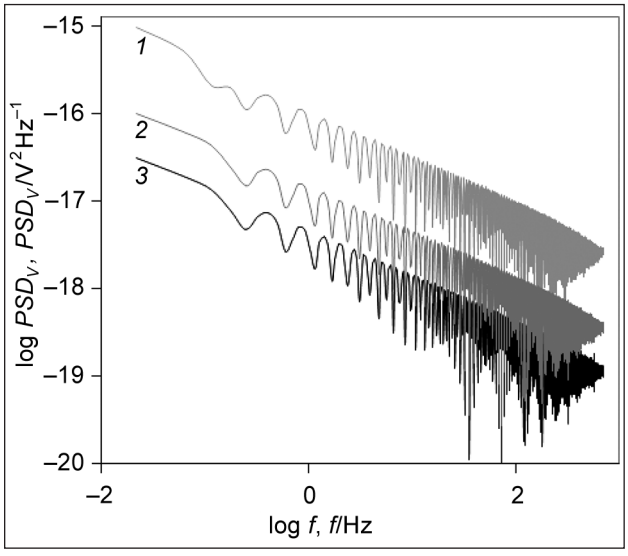

Fig. 7. *PSD* of the voltage noise for palladium electrocrystallization on stainless steel 316L measured at different cathodic current density: *1* – –1.5, *2* – –2.5 and *3* – –4 mA cm^{-2}

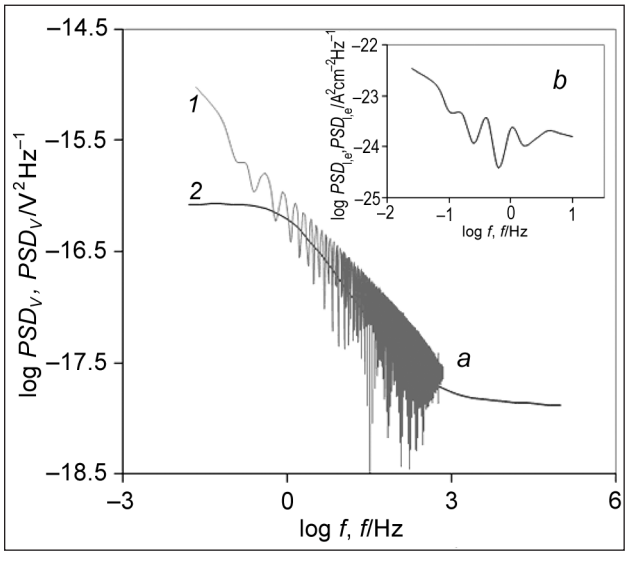

Fig. 8. (*a*) *PSD* of the (*1*) voltage noise compared to that of the (*2*) thermal noise of the electrode impedance at current –1.5 mA cm^{-2}. (*b*) The current fluctuations of $PSD_{I,e}$

fluctuation is observed in PSD plots due to the random birth of edges and therefore nucleation and growth of palladium monolayer's on the surface [48, 51, 63]. PSD plots exhibit a $1/f^n$ dependency in the high and low frequency regions. The PSD plots were fitted to

$$\log PSDv = A_v + S_v \log f, \tag{23}$$

where S_v and A_v are the slope and magnitude of the potential PSD plots, respectively. The PSD parameter S_v has often been related to the mechanism of the process [64], therefore it indicates the presence of just one type of electrocrystallization mechanism in applied cathodic currents. Considering the electrode as a linear system, the PSD of the current fluctuations can be calculated by the relationship [64]:

$$PSD_I = \frac{PSD_v}{|Z|^2}. \tag{24}$$

In Fig. 7 it can be seen that PSD_I is proportional to the applied current in the whole frequency band, which is consistent with the assumption of a shot noise following the Poisson law [65]. A significant comparison of PSD_V to the thermal noise [66] of electrode impedance Z can be made by measuring PSD_V and Z during the experiment. The thermal noise, calculated from the real part $R_{real}(Z)$ of the impedance Z by $4k_BTR_{real}(Z)$, is represented in Fig. 8a and compared with PSD_V where k_B is Boltzmann's constant and T is the absolute temperature. At low frequencies, the thermal noise is a decreasing function of current and it remains lower than the electrochemical noise. At high frequencies PSD_v reduces to thermal noise. Therefore PSD_V can be considered as the sum of a thermal noise and an excess noise $PSD_{v,e}$ which may correspond to the shot noise resulting from the random birth of palladium monolayer

$$PSD_v = 4k_BTR_{real}(Z) + PSD_{v,e}. \tag{25}$$

The $PSD_{I,e}$ of the current fluctuations corresponding to the excess current noise can be calculated by

$$PSD_{I,e} = \frac{PSD_{V,e}}{|Z|^2} \tag{26}$$

and is exhibited in Fig. 8b.

If the birth time t_n follows a Poisson distribution of the parameter m according to Eq. (6), the power spectral density of current fluctuations about the mean current is

$$PSD_I = J^2h^2l_0^2m\left|F(w)\right|^2. \tag{27}$$

Therefore the ratio $PSD_{I,e}/I$ can be calculated from the model by combining (8) and (27):

$$\frac{PSD_{I,e}}{I} = \frac{I|F(w)|^2}{m\tau^2} = hl_0r_0\frac{|F(w)|^2}{\tau^2}. \tag{28}$$

The ratio $PSD_{I,e}/I$ is an increasing function of the current density when taking into account the lengthening of r_0 with increasing overpotential. The low frequency limit of $PSD_{I,e}$ whose expression is

$$PSD_{I,e} = \frac{I^2}{m} \tag{29}$$

offers a particular interest to evaluate the mean birth rate m of the monolayer. It appears in Fig. 8b that this low frequency limit has not been experimentally obtained yet in the explored frequency band. Since $PSD_{I,e}$ is probably higher than the value measured at 15 mHz, it can be concluded from (29) that the birth rate m of the monolayer is lower than 4.7×10^{16} s^{-1} cm^{-2} which was increased with increasing the applied cathodic current.

CONCLUSIONS

Electrocrystallization of palladium onto a steel electrode from 0.01 M $Pd(NH_3)_4Cl_2$, NH_4Cl, and NH_4OH bath was studied by the methods of cyclic voltammetry, impedance spectroscopy and noise analysis. It is shown that electrodeposition of palladium proceeds via nucleation and growth. Palladium deposition implies a multi-step mechanism and takes place through reaction intermediates and nucleation sites.

A theoretical impedance model based on palladium nucleation and growth is proposed which captures and explains all of the features of potential dependence of experimental impedance. The high frequency semi-circle of the complex plane plot is related to charge transfer resistance for Pd^{2+} reduction and the presence of low-frequency features can be interpreted in terms of the relaxations of the electrode area on the basis of an impedance model for the birth and growth of monolayers. In this analysis, the capacitive feature has been ascribed to the propagation of edges over finite distances whereas the inductive feature essentially reflects desorption of inhibiting adsorbates.

The electrochemical noise analysis was used to provide additional information. It clearly appears that the current fluctuations characterized by their *PSD* originate from the random birth of edges and birth rate of monolayers is lower than 4.4×10^{16} s^{-1} cm^{-2}.

Received 4 February 2013
Accepted 18 February 2013

References

1. P. Kumar, L. K. Malhotra, *Mater. Chem. Phys.*, **88**, 106 (2004).
2. C. Milhano, D. Pletcher, *J. Electroanal. Chem.*, **614**, 24 (2008).
3. C. H. Lee, S. C. Wang, C. J. Yuan, M. F. Wen, K. S. Chang, *Biosens. Bioelectron.*, **22**, 877 (2007).
4. H. Naohara, S. Ye, K. Uosaki, *Electrochim. Acta*, **45**, 3305 (2000).
5. H. Naohara, S. Ye, K. Uosaki, *J. Electroanal. Chem.*, **500**, 435(2001).
6. S. C. Chen, G. C. Tu, C. C. Y. Hung, C. A. Huang, M. H. Rei, *J. Membr. Sci.*, **314**, 5 (2008).
7. O. Corduneanu, V. C. Diculescu, A. M. Chiorcea-Paquim, A. M. Oliveira-Brett, *J. Electroanal. Chem.,* **624**, 97 (2008).
8. A. Mourato, J. P. Correia, H. Siegenthaler, L. M. Abrantes, *Electrochim. Acta,* **53**, 664 (2007).
9. I. Danaee, *J. Electroanal. Chem.*, 662, 415 (2011).
10. B. J. Hinch, C. Koziol, J. P. Toennies, G. Zhang, *Vacuum,* **42**, 309 (1991).
11. I. Danaee, F. Shoghi, M. Dehghani Mobarake, M. Kameli, *J. Solid State Electrochem.,* **14**, 57 (2010).
12. M. Baldauf, D. M. Kolb, *Electrochim. Acta,* **38**, 2145 (1993).
13. Z. F. Lodhi, J. M. C. Mol, W. J. Hamer, H. A. Terryn, J. H. W. De Wit, *Electrochim. Acta,* **52**, 5444 (2007).
14. J. L. Ortiz-Aparicio, Y. Meas, G. Trejo, R. Ortega, T. W. Chapman, E. Chainet, P. Ozil, *Electrochim. Acta*, **52**, 4742 (2007).
15. J. Wu, Y. Jiang, C. Johnson, X. Liu, *J. Power Sources,* **177**, 376 (2008).
16. S. E. Nam, S. H. Lee, K. H. Kew-Ho Lee, *J. Membr. Sci.,* **153**, 163 (1999).
17. I. Danaee, M. Jafarian, F. Forouzandeh, F. Gobal, M. G. Mahjani, *Electrochim. Acta*, **53**, 6602 (2008).
18. Y. Wan, Z. Lin, D. Zhang, Y. Wang, B. Hou, *Biosens. Bioelectron.,* **26**, 1959 (2011).
19. I. Danaee, M. Jafarian, F. Forouzandeh, F. Gobal, M. G. Mahjani, *Int. J. Hydrogen Energy*, **33**, 4367 (2008).
20. J. R. Macdonald, *Impedance Spectroscopy*, Wiley, New York (1987).
21. C. Cachet, U. Stroder, R. Wiart, *Electrochim. Acta*, **27**, 903 (1982).
22. C. Cachet, B. Saidani, R. Wiart, *Electrochim. Acta*, **34**, 1249 (1989).
23. C. Cachet, B. Saidani, R. Wiart, *Electrochim. Acta*, **33**, 405 (1988).
24. C. Cachet, B. Saidani, R. Wiart, *J. Electrochem. Soc.*, **138**, 678 (1991).
25. C. Cachet, Z. Chami, R. Wiart, *Electrochim. Acta*, **32**, 465 (1987).
26. T. Chengyu, C. Hang, H. Wei, L. Yu, Z. Ziqiao, *Rare Metal Mat. Eng.*, **39**, 10 (2010).
27. C. Cachet, C. Gabrielli, F. Huet, M. Keddam, R. Wiart, *Electrochim. Acta*, **28**, 899 (1983).
28. M. Fleischmann, S. K. Rangarajan, H. R. Thirsk, *Trans. Faraday Soc.*, **63**, 1240 (1967).
29. M. Fleischmann, S. K. Rangarajan, H. R. Thirsk, *Trans. Faraday Soc.*, **63**, 1251 (1967).
30. M. Fleischmann, S. K. Rangarajan, H. R. Thirsk, *Trans. Faraday Soc.*, **63**, 1256 (1967).
31. S. K. Rangarajan, *J. Electroanal. Chem.*, **17**, 61 (1968).
32. M. Fleischmann, H. R. Thirsk, in: P. Delahay (ed.), *Advanced Electrochemistry and Electrochemical Engineering*, Vol. 3, p. 123, Interscience, New York (1963).
33. S. J. A. Harrison, H. R. Thirsk, in: A. J. Bard (eds.), *Electroanalytical Chemistry*, Vol. 5, p. 67, Marcel Dekker, New York (1971).
34. S. K. Rangarajan, *J. Electroanal. Chem.*, **46**, 125 (1973)
35. R. D. Armstrong, J. A. Harrison, *J. Electrochem. Soc.*, **116**, 328 (1969).
36. R. D. Armstrong, A. A. Metcalfe, *J. Electroanal. Chem.*, **63**, 19 (1975).
37. R. D. Armstrong, A. A. Metcalfe, *J. Electroanal. Chem.*, **71**, 5 (1976).
38. C. Cachet, I. Epelboin, M. Keddam, R. Wiart, *J. Electroanal. Chem.*, **100**, 745 (1979).
39. Z. Stoynov, *Electrochim. Acta*, **35**, 1493 (1990).
40. J. R. Macdonald, *Solid State Ionics*, **58**, 97 (1992).
41. I. Epelboin, M. Joussellin, R. Wiart, *J. Electroanal. Chem.*, **101**, 281 (1979).

42. C. Cachet, M. Froment, R. Wiart, *Electrochim. Acta*, **24**, 713 (1979).
43. I. Epelboin, M. Ksouri, R. Wiart, *J. Electrochem. Soc.*, **122**, 1206 (1975).
44. E. Chassaing, R. Wiart, *Electrochim. Acta*, **29**, 649 (1984).
45. I. Epelboin, R. Wiart, *J. Electrochem. Soc.*, **118**, 1577 (1971).
46. F. Mansfeld, H. Xiao, *J. Electrochem. Soc.*, **140**, 2205 (1993).
47. H. Xiao, F. Mansfeld, *J. Electrochem. Soc.*, **141**, 2332 (1994).
48. G. Blanc, C. Gabrielli, M. Ksouri, R. Wiart, *Electrochim. Acta*, **23**, 337 (1978).
49. Z. Zhang, W. H. Leng, Q. Y. Cai, F. H. Cao, J. Q. Zhang, *J. Electroanal. Chem.*, **578**, 357 (2005).
50. Y. Zhong-Nian, Z. Zhao, L. Wen-Hua, L. Ke, Z. Jian-Qing, *Trans. Nonferrous Met. Soc. China*, **16**, 209 (2006).
51. E. Budevski, V. Obretenov, W. Bostanov, G. Staikov, *Electrochim. Acta*, **34**, 1023 (1989).
52. E. Budevski, V. Bostanov, G. Staikov, *Ann. Rev. Mat. Sci.*, **10**, 85 (1980).
53. I. Danaee, M. Jafarian, F. Forouzandeh, F. Gobal, M. G. Mahjani, *Electrochim. Acta*, **53**, 6602 (2008).
54. I. Danaee, M. Jafarian, F. Forouzandeh, F. Gobal, M. G. Mahjani, *J. Phys. Chem. B*, **112**, 15933 (2008).
55. S. Fletcher, *Electrochim. Acta*, **28**, 917 (1983).
56. S. Fletcher, C. S. Halliday, D. Gates, M. Westcott, T. Lwin, G. Nelson, *J. Electroanal. Chem.*, **159**, 267 (1983).
57. D. R. Salinas, E. O. Cobo, S. G. Garcia, J. B. Bessone, *J. Electroanal. Chem.*, **470**, 120 (1999).
58. M. Jafarian, F. Gobal, I. Danaee, M. G. Mahjani, *Electrochim. Acta,* **52**, 5437 (2007).
59. R. Wiart, *Electrochim. Acta*, **35**, 1587 (1990).
60. M. Jafarian, M. G. Mahjani, F. Gobal, I. Danaee, *J. Electroanal. Chem.*, **588**, 190 (2006).
61. J. R. Macdonald, *Solid State Ionics*, **13**, 147 (1984).
62. A. Maritan, F. Toigo, *Electrochim. Acta*, **35**, 141 (1990).
63. C. Gabrielli, M. Ksouri, R. Wiart, *J. Electroanal. Chem.*, **86**, 233 (1987).
64. C. C. Lee, F. Mansfeld, *Corros. Sci.*, **40**, 959 (1998).
65. F. Huet, in: P. Marcus, F. Mansfeld (eds.), *Analytical Methods in Corrosion Science and Technology*, Ch. 14, CRC Press, Taylor & Francis Group (2006).
66. C. Gabrielli, F. Huet, M. Keddam, *Electrochim. Acta*, **31**, 1025 (1986).

Iman Danaee

PALADŽIO PASLUOKSNĖS NUKLEACIJOS IR AUGIMO ANT NERŪDIJANČIO PLIENO 316L TEORINIAI BEI EKSPERIMENTINIAI TYRIMAI

S a n t r a u k a

Paladžio nukleacija ir augimas iš elektrolito, turinčio 0,01 M $Pd(NH_3)_4Cl_2$, NH_4Cl ir NH_4OH (pH = 10), buvo tiriama ciklinės voltamperometrijos, impedanso spektroskopijos ir elektrocheminio triukšmo metodais.